Article

Symmetry-reduced topological interface for unleashing a multidirectional spin-orbit torque

Check for updates

Satoshi Sugimoto[1], Yasufumi Araki [2], Yukiko K. Takahashi [1], Jun'ichi Ieda [2] & Shinya Kasai [1] ✉

Current-induced spin-orbit torque at heavy metal/ferromagnet interfaces plays a critical role in modern spintronics. The challenges in relevant research are to enhance the conversion efficiency and generate unconventional torque components. Here, we propose a simple protocol to meet such demands by engineering symmetrical structures, specifically by a wedge-shaped topological material interface in Bi_2Te_3/CoFeB heterostructures. The symmetry of the topological interface is manipulated to lead to unconventional emergences of both the out-of-plane and in-plane spin polarizations. Torque measurements show that these polarizations have conversion efficiencies up to 10%, characterized by the nonreciprocal ferromagnetic resonance spectra and the distinctive torque profile. The observed enhancement in the unconventional spin-orbit torque is attributed to the wedge-oriented symmetry reduction of the spin-momentum locking structure of interfacial Dirac fermions. This advance opens avenues for designing geometrically characteristic spintronics devices, demonstrating the potential of using multidirectional spin-orbit torques for forthcoming nanotechnological applications.

A trend of all-electric operation of spintronics devices has resulted from the development of spin-orbit torque (SOT) applications over the last decade[1–4], where high-speed operations with high endurance are principally achievable for memory and logic devices[5] with simple thin-film heterostructures. The development of SOT devices is linked to progress in studies on spin-to-charge conversion. In addition to its conversion efficiency, the direction of spin polarization also plays a crucial role in designing SOT device configurations[6,7]. Manipulation of the spin polarization direction is particularly important in solving the problem of nondeterministic nature in the switching process of perpendicular magnetization[3]. For the conventional spin Hall or Rashba SOT, it vanishes once the magnetization tilts down to the in-plane direction, resulting in uncontrollable final states in the absence of an applied external field. This vanishing of the SOT is caused by the symmetry of the system because rotational and mirror symmetries determine the relation between the current injection and spin polarization directions. Therefore, reduction of symmetry could be used to overcome geometric constraints in SOT applications. At an early stage of development, convoluted device engineering is used to exploit exchange interactions[8,9], interlayer coupling[10], structural asymmetry[11–13], and magnetic anisotropy[14]. The use of noncollinear antiferromagnets (including Mn) in spin-current injection layers has been investigated, where the unconventional exchange coupling at the interface gives rise to an out-of-plane spin polarization[15–17].

There has been considerable interest in using alternative approaches to produce unconventional SOTs by decreasing structural symmetry while maintaining the original heterostructures. A decrease in the rotational and mirror symmetries of the crystalline structure results in a warping of spin-orbit coupling (SOC) pattern in momentum space, leading to a rich variation in spin polarization that is not expected from the conventional SOT from isotropic spin Hall or Rashba effects[18,19]. To date, threefold symmetry has been experimentally observed in several heavy metal compounds, namely, WTe_2[20], $NbSe_2$[21], and $L1_1$-CuPt/CoPt[22], where an SOT from out-of-plane spin polarization has been recently reported. The emergence of such a nontrivial torque component has enabled field-free SOT operation of heavy metal/ferromagnet (HM/FM) heterostructures in several experiments[22–25]. However, the typical amplitude of this SOT remains one order of magnitude smaller than that of the conventional SOT[15–17,20], which hinders the development of SOT for various applications. Therefore, we need to design unconventional SOTs by reducing the symmetries of system, with their magnitudes reaching up to that of the conventional SOT.

In this study, we propose an alternative protocol to generate and enhance unconventional SOT based on symmetry reduction in a topological insulator (TI) material Bi_2Te_3. Bi_2Te_3 shows the spin-momentum locked electronic states on the surface, with the hexagonal warping structure due to the discrete rotational symmetry of crystal[26–28]. From such a warped spin-momentum locking structure, we may expect both the enhancement of the

SOT efficiency[29–31] and the emergence of the unconventional SOT component[32–34]. The pioneering experimental works[35,36] with Bi-based chalcogenides recorded more than 100% efficiencies in their charge-to-spin conversion process, which later enabled the ultralow power SOT switching with double-digit decrease in the critical current density[37]. Numerous studies with TIs were conducted to improve the conversion efficiencies so far, by adjusting TI crystallinity[38] or positioning the Fermi level closer to the Dirac point[39]. On the other hand, its capability as a platform for the unconventional SOTs, which was proposed by several theoretical works, has not been paid attention to in experiments so far.

The essence of this work is to adopt the TI not simply as an efficient source of SOT, but rather as a source of multi-directional SOT components by manipulating its unique symmetry structure. Since the effect of spin-momentum locking in the surface Dirac electrons is much stronger than the conventional Rashba SOC[40,41], electron spin polarization on the TI surface is highly sensitive to symmetry reduction. Therefore, we may expect that the combination of the warping effect from the crystalline structure and the asymmetry of the sample structure can generate unconventional spin polarization of a sizeable magnitude. Here, we manipulate the (001) surface of the TI material Bi_2Te_3, which is originally in the threefold point group C_{3v}[42–45]. We introduce an atomic-scale thickness gradient by synthesizing a wedge-shaped film to reduce the rotational and mirror symmetries of the surface. Film wedging has a marked effect on the TI surface state, resulting in further distortion in the spin-momentum locking structure. By comparing the measurements using Bi_2Te_3/CoFeB heterostructures without and with the film wedging, we report the emergence of multidirectional SOT arising from the film wedging. The unconventional parallel and out-of-plane spin polarizations therein reach up to 50% the conventional component orthogonal to the current flow. In particular, a spin polarization parallel to the current direction is observed in such symmetry-reduced systems, which are principally prohibited in highly symmetric crystals.
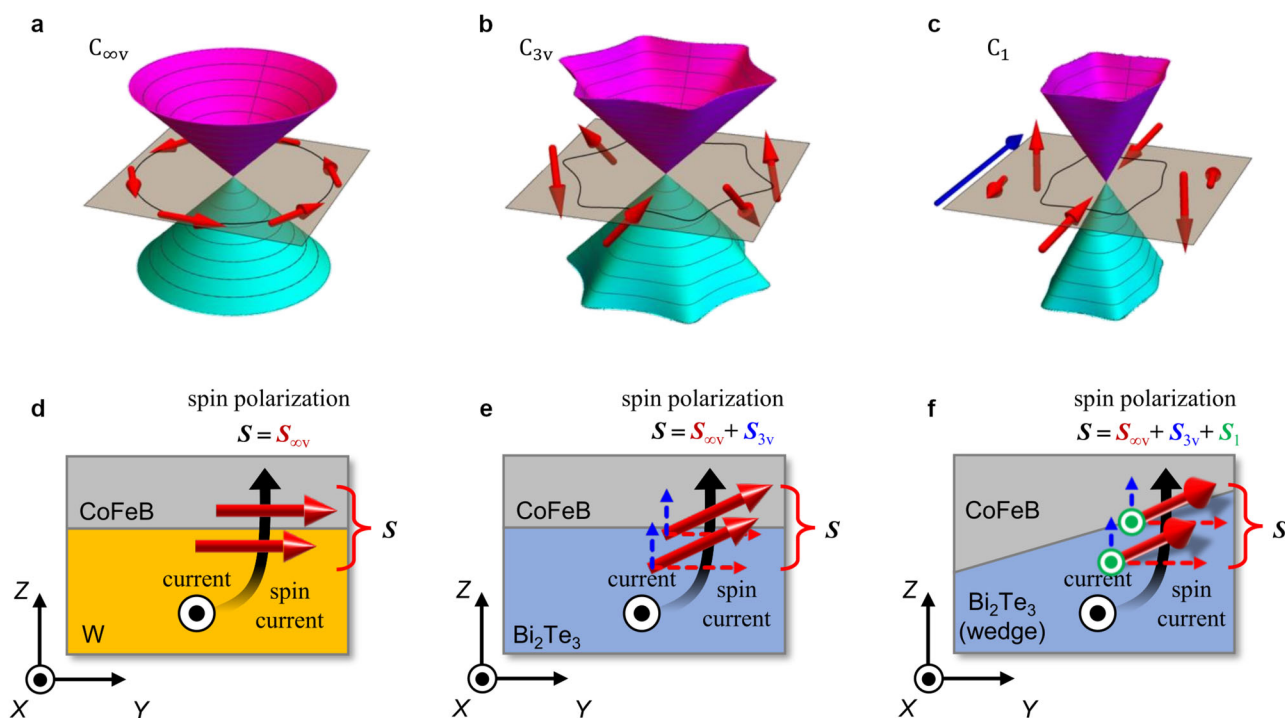
Results and discussion

Symmetry reduction protocol for C_{3v} systems

We briefly discuss the effect of symmetry reduction on the SOT structure in magnetic heterostructures based on group theory analysis in two dimensions (2D). A spin current of a spin polarization **S** that is injected into a magnetic layer in response to an electric field **E** can exert a field-like (FL) SOT $\tau_{FL} \propto \mathbf{m} \times \mathbf{S}$ and a damping-like (DL) SOT $\tau_{DL} \propto \mathbf{m} \times (\mathbf{S} \times \mathbf{m})$ on the magnetization **m**. The possible form of the induced **S** is an axial vector belonging to the irreducible representation in common with the angular momentum, which can be constructed from combinations of **E**, **m**, and any other perturbations applied to the system. Symmetry reduction results in a rich variation in the SOT by decreasing the number of classes of irreducible representations[4,18]. Below, we consider a fixed Cartesian coordinate system (X, Y, Z) for the crystal, where the Z-axis is the rotational symmetry axis (the film normal). We extract some SOT components characteristic of each symmetry group (all possible SOT structures are listed in Supplementary Note 1: Group-theory analysis of spin-orbit torque under wedging).
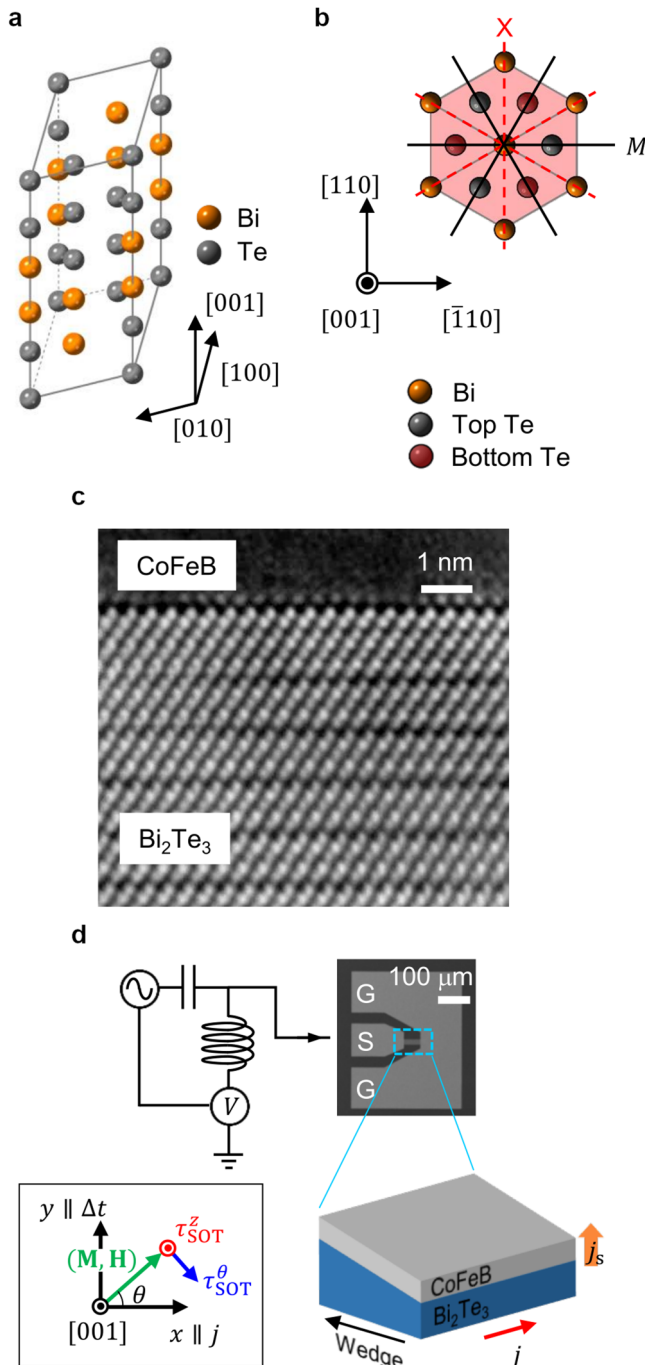
We start from the largest symmetry possible at a 2D interface, the $C_{\infty v}$ group in the continuum, which is symmetric under an arbitrary rotation R_ϕ around the Z-axis and a reflection σ_v by arbitrary mirror planes containing the Z-axis (Fig. 1a). This situation principally applies to polycrystal and amorphous, where the crystal orientations are randomly distributed and integrated out in total. For instance, a Rashba-type SOC with in-plane spin polarization, $\propto (k_X \sigma_Y - k_Y \sigma_X)$, is permitted for this symmetric structure. The linear Dirac-cone dispersion on the TI surface is the typical example in this class. The possible form of **S** induced solely by an in-plane **E** is limited to $\mathbf{S}_{\infty v} \propto \hat{\mathbf{Z}} \times \mathbf{E} = (-E_Y, E_X, 0)$, which is expected from the conventional spin Hall and Rashba-Edelstein effects, as shown in Fig. 1d.

The crystalline structure decreases $C_{\infty v}$ at the interface to a discrete group. Among the discrete point groups in 2D, the C_{3v} structure commonly appears in cubic and hexagonal crystals, including at the (001) topological

Fig. 1 | Schematics of bands and spin distributions under different symmetry group structures at the interface and corresponding current-induced spin polarizations. Schematized structures of the interfacial bands and Fermi surface. **a** Isotropic heterostructures that belong to the $C_{\infty v}$ point group. **b** Heterostructure with threefold rotational symmetry (C_{3v}). **c** C_{3v} heterostructure with film wedging (in the direction **F**), where the point group is reduced to the trivial C_1 group. Schematics of the sample geometry and corresponding spin polarization **S** of the spin-orbit torque (SOT). **d** W/CoFeB heterostructure belonging to $C_{\infty v}$ point group exhibiting only in-plane polarization $\mathbf{S}_{\infty v}$ orthogonal to the current. **e** ferromagnet (FM) and topological insulator (TI) (Bi_2Te_3) heterostructure beonging to C_{3v} point group permitting out-of-plane polarization $\mathbf{S}_{3v}$. **f** FM and wedged TI (Bi_2Te_3) heterostructure beonging to C_1 point group inducing both out-of-plane polarization $\mathbf{S}_{3v}$ and in-plane polarization $\mathbf{S}_1$ parallel to the current.

a

b

c

d

Fig. 2 | Ferromagnetic resonance-based torque measurements obtained under symmetry reduction of the rhombohedral Bi2Te3 (001) surface. a The crystal structure of the rhombohedral Bi_2Te_3. **b** Plane view of the hexagon projected along the [001] direction, where two Bi atomic layers (orange) are sandwiched between four Te atomic layers (the top and bottom layers are shown in gray and red, respectively). For simplicity, only the atoms in the hexagonal region (shaded red) are shown. The mirror symmetry M is present for the $(\bar{1}10)$ plane (black solid line) but is absent for the (110) plane (red dashed line). **c** Cross-sectional high-angle annular dark-field scanning transmission electron microscope (STEM) image of the epitaxial Bi_2Te_3/CoFeB bilayer gazed from Bi_2Te_3-[100] direction. **d** Schematic of the spin torque ferromagnetic resonance (ST-FMR) measurement process for heavy metal/ferromagnet (HM/FM) heterostructures. The device geometry is presented by scanning electron microscope (SEM) image of a Bi_2Te_3/CoFeB bilayer sample. The thickness gradient $\triangle t = (3 \pm 1)$A is set along the y-axis, orthogonal to the current direction (x-axis). An in-plane magnetic field $\mu_0 H$ is applied to 45° from the x-axis to maximize the anisotropic magnetoresistance (AMR) projection. Both the current ($\| x$) and thickness gradient ($\| y$) are applied at the (001) plane of Bi_2Te_3 (the crystalline structure of the sample is detailed in Supplementary Note 3). Measurements with the uniformly thick W/CoFeB and Bi_2Te_3/CoFeB heterostructures are done with the same configuration.

classified as the "3 m torque" and the "planar Hall torque" in preceding theories, respectively[19,32–34]. These types of SOTs have been experimentally reported for the $L1_1$-CuPt/CoPt interface[22].

On this C_{3v} interface, we consider the effect of film wedging. Film wedging can be regarded as an in-plane vector-type perturbation **F** in the direction of the thickness gradient because it transforms under both the R_3 rotations and σ_v reflections but does not break time-reversal symmetry. This perturbation reduces the symmetry group down to the trivial C_1 group. It considerably distorts the structure of the fully spin-momentum-locked Dirac fermions on the TI surface, as shown in Fig. 1c (see Supplemental Note 1 for a detailed discussion). Combinations of **E** and **F** yield unconventional forms of the in-plane and out-of-plane components $\mathbf{S}_1^{\|}$ and $\mathbf{S}_1^{\perp}$, that are not captured in $\mathbf{S}_{\infty v}$ and $\mathbf{S}_{3v}$:

$$\mathbf{S}_1^{\|} \propto \left(E_X F_Y + E_Y F_X\right)\hat{\mathbf{X}} + \left(E_X F_X - E_Y F_Y\right)\hat{\mathbf{Y}}, \ \mathbf{S}_1^{\perp} \propto \left(E_X F_Y - E_Y F_X\right)\hat{\mathbf{Z}},$$
$$(1)$$

where all three spin components are permitted (Fig. 1f). The out-of-plane component $\mathbf{S}_1^{\perp}$ arises if the wedging **F** is designed to be perpendicular to the current injection direction **E**. For instance, if the current is injected in the X-direction, wedging should be introduced in the Y-direction to obtain the out-of-plane component. In this case, the in-plane component $\mathbf{S}_1^{\|}$ becomes parallel to the current injection direction, $\mathbf{S}_1^{\|} \propto E_X F_Y \hat{\mathbf{X}}$. Such a component with the spin polarization along the current direction is not permitted at $O(m^0)$ in either $\mathbf{S}_v$ or $\mathbf{S}_{3v}$. These unconventional SOT components result in the extinction of the geometrically invariant point ($\tau = 0$) during the magnetization switching process. Therefore, the symmetry engineering discussed here could be used to realize deterministic field-free switching. The **F** effect considered here could be applied to model any other in-plane inhomogeneity, e.g., an in-plane temperature gradient or asymmetry between electrodes, although the corresponding effects are not as controllable as those of film wedging.

Measurements of multidirectional SOT at a symmetry-reduced interface

The aforementioned protocols were demonstrated experimentally for the topological surface state of Bi_2Te_3. As Bi_2Te_3 forms a rhombohedral unit cell (Fig. 2a), its (001) surface belongs to the C_{3v} group (Fig. 2b). Figure 2d is a schematic of an atomic-scale thickness gradient in a wedge structure that we prepared in the epitaxial heterostructure of [001]-Bi_2Te_3 and amorphous CoFeB (Fig. 2c). The film thickness in the heterostructure varies by $\triangle t = (3 \pm 1)$A over a channel width of 12 μm. This wedging acts as an in-plane vector perturbation **F**, which reduces the symmetry of the system down to the trivial C_1 group, as discussed in the previous section. We used

interface of Bi_2Te_3. This point group hosts the threefold rotational symmetry R_3 around the Z-axis and the reflection symmetry σ_v by the three mirror planes. We here fix the X- and Y-axes of the Cartesian coordinate system such that the XZ-plane coincides with one of the mirror planes of σ_v. The C_{3v} structure allows a hexagonal warping for the SOC. For the 2D Dirac fermions on the TI surface, the warping effect is parametrized as $\propto \mathrm{Re}\left(k_X + ik_Y\right)^3 \sigma_Z$, producing an unconventional out-of-plane spin polarization on the Fermi surface, as shown in Fig. 1b[4,18,46]. This term can produce an out-of-plane spin component of the SOT, $\mathbf{S}_{3v}^Z \propto (\mathbf{E} \cdot \mathbf{m})\hat{\mathbf{Z}}$, which is allowed in $C_{\infty v}$ but prohibited for the in-plane Rashba SOC. The C_{3v} structure also permits in-plane components of the SOT, $\mathbf{S}_{3v} \propto \left(E_X m_X - E_Y m_Y\right)\hat{\mathbf{X}} + \left(-E_X m_Y - E_Y m_X\right)\hat{\mathbf{Y}}$, in addition to $\mathbf{S}_{\infty v}$ produced by the combination of **E** and **m**. This $\mathbf{S}_{3v}$ makes the emergence of field-like $\boldsymbol{\tau}_{3m} = \tau_{3m}\left(\mathbf{m} \times \mathbf{S}_{3v}\right)$ and damping-like $\boldsymbol{\tau}_{PH} = \tau_{PH}\left[\mathbf{m} \times \left(\mathbf{S}_{3v} \times \mathbf{m}\right)\right]$ possible in C_{3v} heterostructures, which have been

Fig. 3 | Spin torque ferromagnetic resonance voltage spectra for different point group structures. ST-FMR voltage spectra of the in-plane magnetic field $\mu_0 H$ for (**a**), W (3 nm)/CoFeB (5 nm), **b** uniformly thick Bi_2Te_3 (8 nm)/CoFeB (5 nm), and **c** wedge-shaped Bi_2Te_3 (8 nm $+ \triangle t$)/CoFeB (5 nm) heterostructures. $\triangle t$ denoted the film thickness variation as $\triangle t = (3 \pm 1)$A. The corresponding fitted curves of individual heterostructures are plotted at (**d**, **e**, and **f**), respectively. The experimental data are shown as closed ($\mu_0 H > 0$) and open ($\mu_0 H < 0$) black symbols, and the fitted curves for $\mu_0 H > 0$ ($\mu_0 H < 0$) are shown in red (magenta) for the symmetric part V_{Sym} and blue (cyan) for the antisymmetric part V_{Asym}. The sign of $\mu_0 H$ is defined to be consistent with the sign of the x-component of $\mu_0 H$.
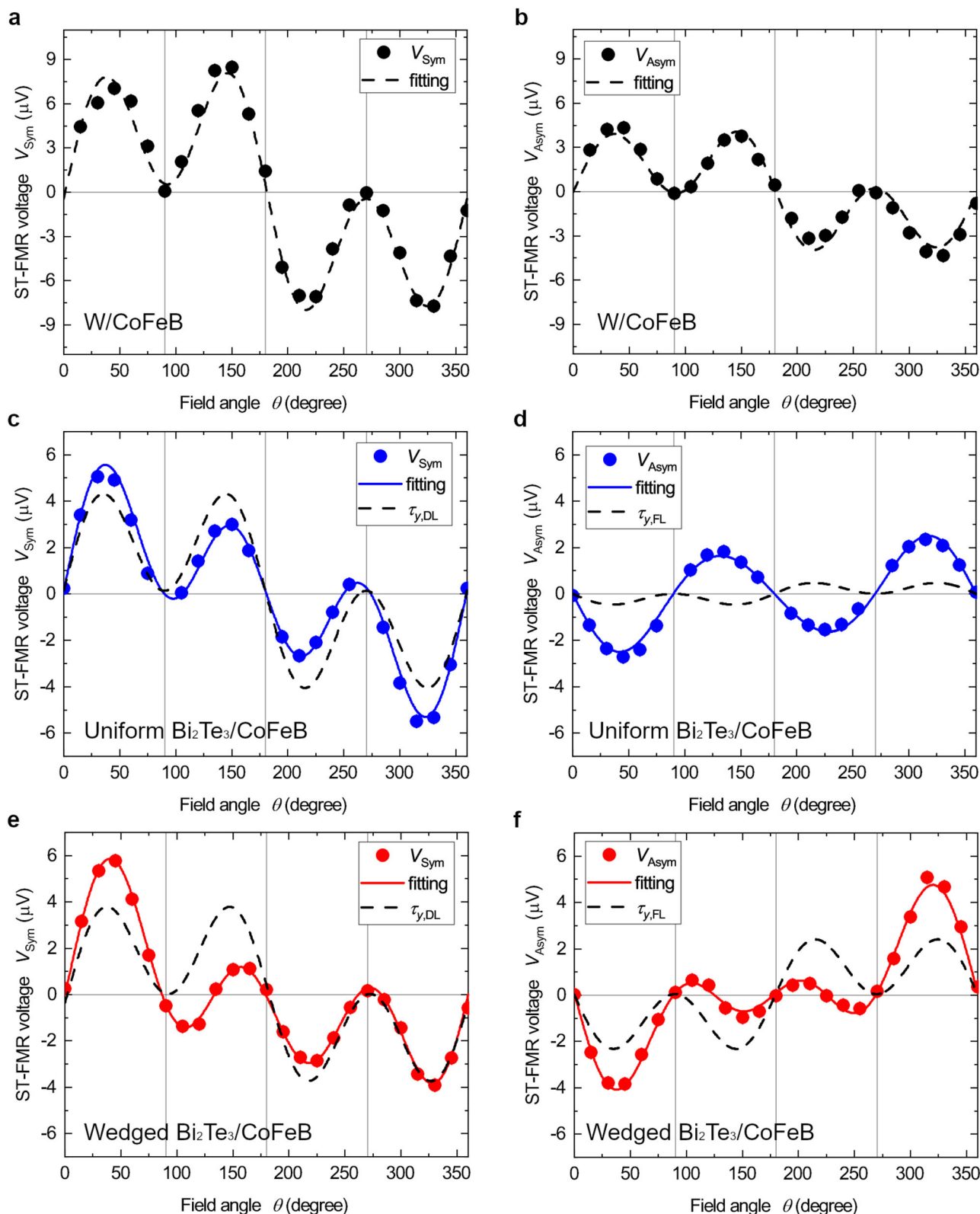
spin-torque ferromagnetic resonance (ST-FMR) to evaluate the SOT components in this heterostructure[2,47]. Distinct from the crystalline coordinate system (X, Y, Z), we describe the laboratory frame by the Cartesian coordinate system (x, y, z), where the x- and y-axes correspond to the directions of the current injection (**j**, or **E**) and wedging (**F**), respectively. To identify the effect of symmetry reduction on the SOTs, we performed the same measurements on two different samples: polycrystalline W/CoFeB (belonging to $C_{\infty v}$) and Bi_2Te_3/CoFeB with a uniform thickness (belonging to C_{3v}).

Figure 3a–c presents the ST-FMR voltage spectra, V_{ST-FMR}, recorded for the three types of prepared heterostructures, where the x-component of the magnetic field is either parallel ($\mu_0 H > 0$) or antiparallel ($\mu_0 H < 0$) to the current direction. The ST-FMR spectrum of the W/CoFeB heterostructure has a reciprocal structure, where inversion of the field direction flips the sign of the signal, indicating a conventional SOT structure (Fig. 3a). By contrast, the spectra of the Bi_2Te_3/CoFeB heterostructures exhibit clear nonreciprocity against field inversion, where an asymmetric large peak in V_{ST-FMR} for $\mu_0 H > 0$ switches to a tiny dip for $\mu_0 H < 0$ (Fig. 3b, c). Moreover, these nonreciprocal FMR spectra vary depending on whether there is wedging in the Bi_2Te_3 film. The antisymmetric component under $\mu_0 H < 0$ almost vanishes at the wedge-shaped interface (see the cyan line in Fig. 3f) but remains finite in the uniformly thick heterostructure (Fig. 3e). The nonreciprocities observed here can be ascribed to the emergence of an asymmetric SOT unique to the Bi_2Te_3/CoFeB heterostructures. To quantify the thermal effects from the Joule heating, we also performed the ST-FMR measurements with lower power excitations. They showed the spectra with their shapes almost consistent with those in Fig. 3, which implies that the thermal effects give only quantitative differences (see Supplementary Note 6: Effects of thermal components).

To obtain a full picture of the SOT, we performed ST-FMR measurements with varying the direction of the in-plane magnetic field. Figure 4 shows the profiles of the symmetric and antisymmetric ST-FMR voltage components, V_{Sym} and V_{Asym}, as functions of the in-plane angle θ of the field direction measured from the current-injection direction (x-axis), as shown in the inset of Fig. 2d. These plots are shown for the conventional W/ CoFeB system in Fig. 4a, b, for the uniformly thick Bi_2Te_3/CoFeB system in Fig. 4c, d, and for the wedge-shaped Bi_2Te_3/CoFeB system in Fig. 4e, f. The conventional SOT for the $C_{\infty v}$ point group results in simple forms[48], such that $V_{Sym(Asym)}(\theta) \propto \sin 2\theta \cos \theta$. These simple forms are shown as black dashed lines in Fig. 4a–f. For W/CoFeB, the simple forms are in excellent agreement with the observed profiles, as shown in Fig. 4a, b. However, the observed profiles of $V_{Sym(Asym)}(\theta)$ both the uniformly thick and wedge-shaped Bi_2Te_3/CoFeB heterostructures are considerably more complex and do not correspond to simple $\sin 2\theta \cos \theta$ functions, as shown in Fig. 4c–f. The $\sin 2\theta \cos \theta$ function is symmetric for $\theta = 90°, 270°$ and antisymmetric for $\theta = 0°, 180°$. By comparison, the observed profiles of V_{Sym} exhibit minor deviations from this behavior, and those of V_{Asym} are entirely different. Such discrepancies are considerably greater for the wedge-shaped samples (Fig. 4e, f) than for the uniformly thick samples (Fig. 4c, d). These differences can be attributed to the unconventional spin polarizations which are permitted by the hexagonal warping and film wedging, as has been discussed in the previous section.
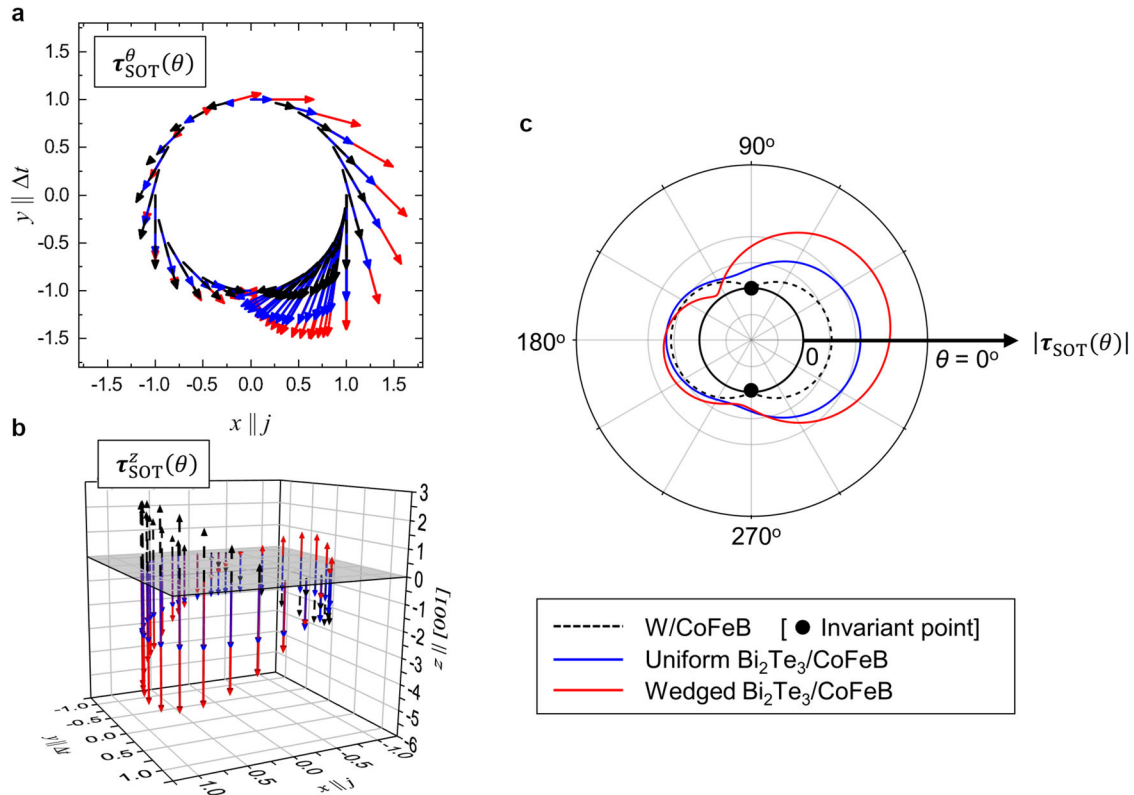
To understand the unconventional spin polarizations from the reduced symmetries, we here decompose the observed profiles of $V_{Sym(Asym)}(\theta)$ into the components of SOT. Incorporating FL and DL components $(\tau_{i,FL}, \tau_{i,DL})$ in each spin direction ($i = x, y, z$) and 3 m and planar Hall components (τ_{3m}, τ_{PH}), the field-angle dependence of the torque components becomes, $\boldsymbol{\tau}_{SOT}(\theta) = \tau_{SOT}^\theta(\theta)\hat{\boldsymbol{\theta}} + \tau_{SOT}^z(\theta)\hat{\mathbf{z}}$, where

Fig. 4 | Angular dependence of spin-torque ferromagnetic resonance signals observed for heterostructures in different point groups. The symmetric (V_{Sym}) and antisymmetric (V_{Asym}) components of the rectified voltage are plotted as functions of the in-plane magnetic field angle θ measured from the current injection direction, as determined from ST-FMR measurements for (a, b), W (3 nm)/CoFeB (5 nm), (c, d), uniformly thick Bi_2Te_3 (8 nm)/CoFeB (5 nm) and (e, f), wedge-shaped Bi_2Te_3 (8 nm + $\triangle t$)/CoFeB (5 nm) heterostructures. The black dashed lines in (a–f) are fitted curves including only the conventional spin polarization components ($\tau_{y,DL(FL)}$). The extended fitting results are based on Eqs. (2) and (3), including both the conventional and unconventional components of SOT ($\tau_{x,DL(FL)}$, $\tau_{y,DL(FL)}$, $\tau_{z,DL(FL)}$), are shown as blue (c, d) and red (e, f) solid lines.

Fig. 5 | Angular profiles of multidirectional spin-orbit torque components observed for heterostructures in different point groups. Angular profiles of (**a**) in-plane SOT $\tau_{SOT}^{\theta}(\theta)$ and **b** out-of-plane SOT $\tau_{SOT}^{z}(\theta)$ for W/CoFeB (black dashed arrows), uniformly thick Bi_2Te_3/CoFeB (blue solid arrows), and wedge-shaped Bi_2Te_3/CoFeB heterostructures (red solid arrows). Each arrow indicates the direction of each SOT component at the angle θ. The gray plane in (**b**) represents $\tau_{SOT}^{z}(\theta) = 0$. **c** Angular profile of the SOT norm $|\tau_{SOT}(\theta)|$ in polar coordinates for the three heterostructures shown in (**a**, **b**). The inner black solid circle represents $|\tau_{SOT}(\theta)| = 0$. Only the W/CoFeB heterostructure shows $|\tau_{SOT}(\theta)| = 0$ where the black dashed curve touches the inner circle (shown by the positions of the black dots), corresponding to the invariant points of the SOT.

$\tau_{SOT}^{\theta}(\theta) = \tau_{x,DL}\sin\theta - \tau_{y,DL}\cos\theta - \tau_{z,FL} + \tau_{PH}\sin 2\theta$ and $\tau_{SOT}^{z}(\theta) = -\tau_{x,FL}\sin\theta + \tau_{y,FL}\cos\theta - \tau_{z,DL} - \tau_{3m}\sin 2\theta$ (the derivation is given in Supplementary Note 2: Field-direction dependence of the ST-FMR signals). Substituting these expressions into $V_{Sym(Asym)}(\theta)$ yields[17,49]

$$V_{Sym} \propto \sin 2\theta\,\tau_{SOT}^{\theta}(\theta), \quad (2)$$

$$V_{Asym} \propto \sin 2\theta\,\tau_{SOT}^{z}(\theta). \quad (3)$$

The measured $V_{Sym(Asym)}(\theta)$ can be consistently fitted by these equations. We note that $\tau_{SOT}(\theta)$ is also affected by the back reaction from the spin pumping and the inverse Edelstein effect. Once their contributions are taken into account, the estimated value of $\tau_{y,DL}$ will be quantitatively shifted (see Supplementary Note 4: Contributions of spin pumping and the inverse Edelstein effect), while the estimations of the other unconventional SOT terms are left unchanged. The fitted results are shown by the solid lines in Fig. 3a–d, with the coefficients provided in Table SIII in Supplementary Note 5: Coefficients for the anisotropic SOT components. These fits produce $\tau_{x(z),DL}$ and $\tau_{x(z),FL}$ with sizable magnitudes, which are approximately 10–50% of that of $\tau_{y,DL(FL)}$, which implies that the unconventional SOT components are significantly induced by the symmetry reduction. The strong out-of-plane torques $|\tau_{z,DL(FL)}|$ comparable to $|\tau_{y,DL}|$ for both the uniformly thick and wedged heterostructures are attributed to the violation of the continuous rotational symmetry at the Bi_2Te_3/CoFeB interface. We note that the uniform thickness Bi_2Te_3 also shows a finite $|\tau_{z,DL(FL)}| \neq 0$, typically at film thickness thinner than 10 nm (See Supplementary Note 3: Microstructure analysis for Bi_2Te_3/CoFeB heterostructures). The sputtered thicker films include more crystalline imperfections, twinning, and/or c-axis misalignments, which tend to obscure $|\tau_{z,DL(FL)}|$ arising from the bulk C_{3V}

structure. Our 8 nm thickness samples are designed to be thin enough to relatively avoid those obstacles.

The SOTs from the spin polarizations parallel to the current direction, $\tau_{x,DL}$ and $\tau_{x,FL}$, are only observed in the wedge-shaped sample. This type of parallel spin polarization is principally prohibited under threefold rotational and mirror symmetries, as discussed in the previous section. The emergence of these two distinct SOT components was confirmed by measurements of current-induced magnetization switching processes and the second-harmonic Hall resistivity (details are provided in Supplementary Note 7: In-plane magnetization switching process by nonreciprocal SOT in Bi_2Te_3/CoFeB heterostructure, Supplementary Note 8: Domain nucleation process underlying in-plane magnetization switching in Bi_2Te_3/CoFeB heterostructure, and Supplementary Note 9: Second-harmonic Hall measurements for Bi_2Te_3/CoFeB heterostructures). These results show that the symmetry reduction by atomic-scale modulation of the thickness of Bi_2Te_3/CoFeB produces unconventional parallel and out-of-plane spin polarizations for the SOT.

These unconventional spin polarization components lead to anisotropy in the SOT, which eliminates the invariant points satisfying $\tau_{SOT}(\theta) = 0$. To visualize these invariant points, we present vector plots of the angular profiles of the in-plane $\tau_{SOT}^{\theta}(\theta)$ and out-of-plane $\tau_{SOT}^{z}(\theta)$ components of the SOTs in Fig. 5a, b, respectively. The SOT profile is symmetric for the W/CoFeB heterostructure (shown as black dashed arrows) but highly asymmetric for both the uniform and wedged heterostructures of Bi_2Te_3/CoFeB (as shown by the blue and red solid arrows, respectively). The magnitude of the in-plane component $\tau_{SOT}^{\theta}(\theta)$ for the wedged heterostructure (Fig. 5a) is almost twice as large for $H_x > 0$ ($-90° \leq \theta \leq 90°$) as for $H_x < 0$ ($90° \leq \theta \leq 270°$). The out-of-plane component $\tau_{SOT}^{z}(\theta)$ also exhibits large anisotropy (Fig. 5b), which evidences the emergence of a sizable out-of-plane spin component induced at the microwedged topological interface. As a result of these asymmetries, the

SOT magnitude $|\boldsymbol{\tau}_{SOT}(\theta)|$ also becomes anisotropic, as shown by the polar plot in Fig. 5c. To clearly show this result, $|\boldsymbol{\tau}_{SOT}(\theta)|$ for each heterostructure is rescaled by a certain factor, where the origin $|\boldsymbol{\tau}_{SOT}(\theta)| = 0$ is represented by the inner black solid circle. Whereas the plot for the W/CoFeB heterostructure includes invariant points touching the $|\boldsymbol{\tau}_{SOT}(\theta)| = 0$ circle at $\theta = 90°$ and $270°$, both the uniformly thick and wedge-shaped Bi_2Te_3/CoFeB heterostructures exhibit nonzero $|\boldsymbol{\tau}_{SOT}(\theta)| \neq 0$ for any θ, indicating the elimination of the invariant points. This behavior facilitates the deterministic switching of magnetization because the SOT remains finite anywhere during the switching process. This capability is attributed to the emergence of unconventional spin polarization components, which are the direct consequence of the symmetry reduction of the topological surface state.

Differences between unconventional and conventional SOTs

For the multidirectional SOT in the symmetry-reduced heterostructure, the spin-to-charge conversion efficiency[6,7,49] should be extended to the multi-component quantities $\boldsymbol{\xi}_{s,DL}$ and $\boldsymbol{\xi}_{s,FL}$ as

$$\boldsymbol{\xi}_{s,DL} = \frac{eM_s t_{FM} t_{TI}}{\hbar} \sqrt{1 + \frac{M_{eff}}{\mu_0 H_0}} \times \begin{pmatrix} \tau_{x,DL}/\tau_{y,FL} \\ \tau_{y,DL}/\tau_{y,FL} \\ \tau_{z,DL}/\tau_{y,FL} \end{pmatrix}, \qquad (4)$$

$$\boldsymbol{\xi}_{s,FL} = \frac{eM_s t_{FM} t_{TI}}{\hbar} \sqrt{1 + \frac{M_{eff}}{\mu_0 H_0}} \times \begin{pmatrix} \tau_{x,FL}/\tau_{y,FL} \\ 1 \\ \tau_{z,FL}/\tau_{y,FL} \end{pmatrix}, \qquad (5)$$

where e is the elementary charge, M_s is the saturation magnetization of the FM layer, t_{FM} and t_{TI} are the thicknesses of the FM and Bi_2Te_3 layers, respectively, and M_{eff} is the effective magnetization (see Methods). Charge-to-spin conversion occurs mainly at the 2D interface in the Bi_2Te_3/CoFeB heterostructures. The efficiency of the y-component of the FL SOT (the leading component arising in the $C_{\infty v}$ group), $\xi_{y,FL}$, is normalized to unity. The extended conversion efficiencies from the wedged heterostructure are quantified relative to $\xi_{y,FL}$ as $(\xi_{x,DL}, \xi_{y,DL}, \xi_{z,DL}) = (-0.07 \pm 0.01, 0.24 \pm 0.02, -0.10 \pm 0.01)$ and $(\xi_{x,FL}, \xi_{z,FL}) = (-0.02 \pm 0.00, 0.08 \pm 0.01)$.

The scale of the multidirectional spin-to-charge conversion efficiency obtained above is considerably large because of the symmetry-reduced spin-momentum locking on the Dirac surface states. This result is demonstrated in Table 1, in which the conversion efficiencies ξ_i ($i = x, y, z$) obtained for the wedged Bi_2Te_3/CoFeB heterostructure herein are compared with those reported in previous experimental studies on unconventional SOT components. Except for the conventional component along the y direction[50,51] ($|\xi_{y,DL}| \gg 0.2$), there are considerable differences in the efficiencies of the in-plane (x) and out-of-plane (z) components. We find a notable in-plane DL torque efficiency $|\xi_{x,DL}| \sim 0.1$, corresponding to the spin component parallel to the current direction, which has never been reported in ordinary

HM/FM heterostructures due to the limitation by the rotational symmetry at the interface. Since this effect is not present in our uniform-thickness sample, we identify its origin not as sample imperfections, but solely as our symmetry reduction protocol. The highest values for this component reported to date have been achieved in structurally engineered devices, i.e., field-annealed W/CoFeB heterostructures with canted easy axes[52] and ultrathin [Pt/Co] multilayers[53]. In contrast, our wedged Bi_2Te_3/CoFeB heterostructure exhibits $|\xi_{x,DL}|$ comparable to those champion records of structurally engineered devices, even though its structural modulation is much simple with an atomic-scale thickness gradient. In addition to the x-component, the out-of-plane DL and FL torque efficiencies, $|\xi_{z,DL}| \sim |\xi_{z,FL}| \sim 0.1$, are also greater than those in previous reports using noncolinear antiferromagnets[15–17] and structural engineering devices[49,53] ($|\xi_{z,FL}| \sim 0.01$). We speculate that a possible origin of such an enhancement of $|\xi_{z,DL(FL)}|$ is the atomic-scale thickness modulation that is not exactly in the C_{3v} structure. As given by Eq. (1), the thickness modulation, represented by the perturbation $\boldsymbol{F}$, also yields an additional contribution to the out-of-plane spin component. Our measurement results imply that the combination of the atomic-scale thickness modulation with the strong spin-momentum locking structure unique to the Dirac surface state of a TI is a powerful tool for inducing multidirectional SOT.

Our protocol for reducing the symmetry of the topological surface state can be regarded as producing an ultimate form of the low-symmetry spin torques with sizable magnitudes, by breaking the crystalline symmetries in materials with strong SOC. This strategy has been developed over the last several years[18,20], and the results of this study demonstrate an alternative route for manipulating the spin polarization in SOTs. Compared with previous engineering approaches, our approach to generate the multi-directional SOT is implemented with a rather simple design with a micro-wedge structure, which can operate with good stability and endurance in devices. Moreover, $(00l)$-oriented Bi-chalcogenide thin films are formed by the weak van der Waals interactions between the adjacent the quintuple layers, and hence they can be deposited onto various substrates with different fabrication techniques[54–56]. From these features, our approach may be compatible toward the future industrial applications combined with developments of in-plane perturbation application methodologies, a pronounced wedge designing, or the glancing angle deposition (GLAD)[57], etc. The concept of symmetry reduction is innovative and can be adapted without degrading the magneto-transport properties of the original devices. Thus, symmetry reduction widens the range of approaches that can be applied to forthcoming magnetic-memory technology and logic devices.

Methods

Sample preparation

The Bi_2Te_3 (8.0–8.3 nm)/$Co_{20}Fe_{60}B_{20}$ (5 nm)/Ru (2 nm) multilayer was grown on a (001)-oriented sapphire Al_2O_3 substrate by DC magnetron sputtering. The Al_2O_3(001) substrate was first annealed above 1000°C for 2 hours to obtain an atomically flat surface. The substrate was then quickly moved to the sputtering chamber, and a rhombohedral Bi_2Te_3 layer was sputtered at 2.1 As^{-1} using a $Bi_2Te_{3.8}$ alloy target. An atomic thickness gradient was created using a moving shutter during the sputtering process. Subsequent in situ annealing was performed at 360°C for 1 hour. It was confirmed that excess Te atoms had evaporated during the sputtering process. The formation of the stoichiometric Bi_2Te_3 film was confirmed by X-ray diffraction (XRD) and inductively coupled plasma–mass spectrometry analysis. The remaining ferromagnetic CoFeB layer and Ru capping layer were sputtered at room temperature.

The Bi_2Te_3/CoFeB heterostructures were patterned into bars with widths of 2–40 μm, and Ta/Au electrodes for RF injection and electrodes were subsequently fabricated using electron beam lithography (EBL) and photolithography.

Film characterization

Transport in and the microstructure of the film were evaluated using XRD, resistivity measurements, atomic force microscopy, scanning electrode

Table 1 | Spin-to-charge conversion efficiencies of various HM/FM heterostructures with unconventional polarization

Material	$\xi_{x,DL}$	$\xi_{y,DL}$	$\xi_{z,DL}$	$\xi_{x,FL}$	$\xi_{z,FL}$
Bi_2Te_3/CFB (this study)	−0.07	0.24	−0.10	−0.02	0.08
WTe_2 ref. 20		0.03	0.013		0.0325
Mn_3SnN ref. 15			0.003		0.053
Mn_3GaN ref. 17	−0.013	0.025	0.019		−0.15
$MnPd_3$ ref. 16	0.017	0.41	0.011		
[Pt/Co]$_5$/Mg/CoFeB ref. 53	−0.083	−0.102	−0.033		
Ta/CoFeB/TaO$_x$ ref. 11		0.58			
FM/Ti/CoFeB/MgO ref. 13		−0.048			
MgO/Py/MgO ref. 49		0.018	0.047		

microscopy (SEM), and high-angle annular dark-field scanning transmission electron microscopy. The detailed results are presented in Supplementary Note 3.

The resistivity of the sputtered Bi_2Te_3 8-nm-thick film used for the experiments was measured as $320 \pm 20\,\mu\Omega\,cm$. The resistivity of the amorphous CoFeB in our devices exceeded $100\,\mu\Omega\,cm$, indicating that sufficient RF current flowed through the bottom Bi_2Te_3 layer. The magnetic properties of the Bi_2Te_3/CoFeB heterostructures were estimated from FMR spectra using the Kittel model. An effective saturation magnetization M_{eff} of $(120.2 \pm 2.4)\,mT$ was determined by fitting the Kittel model to the FMR spectra. The field misalignment was estimated to be less than 0.3 mT from the symmetry of the spectra.

Measurements

The ST-FMR measurements were carried out by applying a microwave current at a fixed frequency (in the 7–15 GHz range) to the Bi_2Te_3/CoFeB bilayer. The lock-in technique with amplitude modulation at 1317 Hz was utilized to improve the signal sensitivity. A rotatable electromagnet was prepared and used to determine the angle-dependent torque presented in Fig. 3a–d. Magnetic fields were swept from $+0.28\,T$ to $-0.27\,T$ to drive the CoFeB through its resonance state. The transmission and reflection coefficients for the RF cables and devices were calibrated by using vector network analyzer measurements in the relevant frequency range. A microwave frequency of 15 GHz and an applied microwave power of 15 dBm were used to obtain the results shown in Figs. 2 and 3. The detected voltage V_{ST-FMR} was divided into symmetric and antisymmetric components (V_{Sym}, V_{Asym}) via resonance spectral fitting as follows:

$$V_{ST-FMR} = V_{Sym}\frac{\triangle H^2}{\triangle H^2 + \left(H - H_0\right)^2} + V_{Asym}\frac{\triangle H\left(H - H_0\right)}{\triangle H^2 + \left(H - H_0\right)^2},$$

where $\triangle H$ denotes the peak width and H_0 represents the resonance field.

Data availability

The data used to generate the plots presented in this paper and other results are available from the corresponding author upon reasonable request.

References

1. Manchon, A. & Zhang, S. Theory of spin torque due to spin-orbit coupling. *Phys. Rev. B* **79**, 094422 (2009).
2. Liu, L., Moriyama, T., Ralph, D. C. & Buhrman, R. A. Spin-torque ferromagnetic resonance induced by the spin Hall effect. *Phys. Rev. Lett.* **106**, 036601 (2011).
3. Miron, I. M. et al. Perpendicular switching of a single ferromagnetic layer induced by in-plane current injection. *Nature* **476**, 189–193 (2011).
4. Manchon, A. et al. Current-induced spin-orbit torques in ferromagnetic and antiferromagnetic systems. *Rev. Mod. Phys.* **91**, 035004 (2019).
5. Aradhya, S. V., Rowlands, G. E., Oh, J., Ralph, D. C. & Buhrman, R. A. Nanosecond-timescale low energy switching of in-plane magnetic tunnel junctions through dynamic oersted-field-assisted spin Hall effect. *Nano Lett.* **16**, 5987–5992 (2016).
6. Dyakonov, M. I. & Perel, V. I. Current-induced spin orientation of electrons in semiconductors. *Phys. Lett. A* **35**, 459 (1971).
7. Hirsch, J. E. Spin Hall effect. *Phys. Rev. Lett.* **83**, 1834 (1999).
8. Oh, Y. W. et al. Field-free switching of perpendicular magnetization through spin–orbit torque in antiferromagnet/ferromagnet/oxide structures. *Nat. Nanotechnol.* **11**, 878–884 (2016).
9. Fukami, S., Zhang, C., DuttaGupta, S., Kurenkov, A. & Ohno, H. Magnetization switching by spin–orbit torque in an antiferromagnet–ferromagnet bilayer system. *Nat. Mater.* **15**, 535–541 (2016).
10. Lau, Y. C., Betto, D., Rode, K., Coey, J. M. D. & Stamenov, P. Spin–orbit torque switching without an external field using interlayer exchange coupling. *Nat. Nanotechnol.* **11**, 758–762 (2016).
11. Yu, G. et al. Switching of perpendicular magnetization by spin–orbit torques in the absence of external magnetic fields. *Nat. Nanotechnol.* **9**, 548–554 (2014).
12. Wu, H. et al. Chiral symmetry breaking for deterministic switching of perpendicular magnetization by spin–orbit torque. *Nano Lett.* **21**, 515–521 (2021).
13. Baek, S.-H. C. et al. Spin currents and spin–orbit torques in ferromagnetic trilayers. *Nat. Mater.* **17**, 509–513 (2018).
14. You, L., Lee, O., Bhowmik, D. & Salahuddin, S. Switching of perpendicularly polarized nanomagnets with spin-orbit torque without an external magnetic field by engineering a tilted anisotropy. *Proc. Natl. Acad. Sci. USA* **112**, 10310–10315 (2015).
15. You, Y. et al. Cluster magnetic octupole induced out-of-plane spin polarization in antiperovskite antiferromagnet. *Nat. Commun.* **12**, 6524 (2021).
16. DC, M. et al. Observation of anti-damping spin–orbit torques generated by in-plane and out-of-plane spin polarizations in $MnPd_3$. *Nat. Mater.* **22**, 591–598 (2023).
17. Nan, T. et al. Controlling spin current polarization through non-collinear antiferromagnetism. *Nat. Commun.* **11**, 4671 (2020).
18. Železný, J. et al. Spin-orbit torques in locally and globally noncentrosymmetric crystals: antiferromagnets and ferromagnets. *Phys. Rev. B* **95**, 014403 (2017).
19. Ovalle, D. G., Pezo, A. & Manchon, A. Spin-orbit torque for field-free switching in C_{3v} crystals. *Phys. Rev. B* **107**, 094422 (2023).
20. MacNeill, D. et al. Control of spin–orbit torques through crystal symmetry in WTe_2/ferromagnet bilayers. *Nat. Phys.* **13**, 300–305 (2017).
21. Guimarães, M. H., Stiehl, G. M., MacNeill, D., Reynolds, N. D. & Ralph, D. C. Spin–orbit torques in $NbSe_2$/permalloy bilayers. *Nano Lett.* **18**, 1311–1316 (2018).
22. Lee, S. et al. Symmetry-dependent field-free switching of perpendicular magnetization. *Nat. Nanotechnol.* **16**, 277–282 (2021).
23. Shi, S. et al. All-electric magnetization switching and Dzyaloshinskii–Moriya interaction in WTe_2/ferromagnet heterostructures. *Nat. Nanotechnol.* **14**, 945–949 (2019).
24. Xie, Q. et al. Field-free magnetization switching induced by the unconventional spin–orbit torque from WTe_2. *APL Mater.* **9**, 051114 (2021).
25. Kao, I.-h. et al. Deterministic switching of a perpendicularly polarized magnet using unconventional spin–orbit torques in WTe_2. *Nat. Mater.* **21**, 1029–1034 (2022).
26. Fu, L., Kane, C. L. & Mele, E. J. Topological insulators in three dimensions. *Phys. Rev. Lett.* **98**, 106803 (2007).
27. Hasan, M. Z. & Kane, C. L. Colloquium: topological insulators. *Rev. Mod. Phys.* **82**, 3045 (2010).
28. Ando, Y. Topological insulator materials. *J. Phys. Soc. Jpn.* **82**, 102001 (2013).
29. Kondou, K. et al. Fermi-level-dependent charge-to-spin current conversion by Dirac surface states of topological insulators. *Nat. Phys.* **12**, 1027–1031 (2016).
30. Wu, C. N. et al. Strongly enhanced spin current in topological insulator/ferromagnetic metal heterostructures by spin pumping. *J. Appl. Phys.* **117**, 17D148 (2015).
31. Gupta, S., Kanai, S., Matsukura, F. & Ohno, H. Ferromagnetic resonance spectra of Py deposited on $(Bi_{1-x}Sb_x)_2Te_3$. *AIP Adv.* **7**, 055919 (2017).
32. Kurebayashi, D. & Nagaosa, N. Theory of current-driven dynamics of spin textures on the surface of a topological insulator. *Phys. Rev. B* **100**, 134407 (2019).
33. Li, J.-Y., Wang, R.-Q., Deng, M.-X. & Yang, M. In-plane magnetization effect on current-induced spin-orbit torque in a ferromagnet/topological insulator bilayer with hexagonal warping. *Phys. Rev. B* **99**, 155139 (2019).

34. Imai, Y., Yamaguchi, T., Yamakage, A. & Kohno, H. Spintronic properties of topological surface Dirac electrons with hexagonal warping. *Phys. Rev. B* **103**, 054402 (2021).

35. Fan, Y. et al. Magnetization switching through giant spin–orbit torque in a magnetically doped topological insulator heterostructure. *Nat. Mater.* **13**, 699–704 (2014).

36. Mellnik, A. R. et al. Spin-transfer torque generated by a topological insulator. *Nature* **511**, 449–451 (2014).

37. Wu, H. et al. Spin-orbit torque switching of a nearly compensated ferrimagnet by topological surface states. *Adv. Mater.* **31**, 1901681 (2019).

38. DC, M. et al. Observation of high spin-to-charge conversion by sputtered bismuth selenide thin films at room temperature. *Nano Lett.* **19**, 4836–4844 (2019).

39. Longo, E. et al. Exploiting the close-to-dirac point shift of the Fermi level in the Sb_2Te_3/Bi_2Te_3 topological insulator heterostructure for spin-charge conversion. *ACS Appl. Mater. Interfaces* **15**, 50237–50245 (2023).

40. Hsieh, X. et al. A tunable topological insulator in the spin helical Dirac transport regime. *Nature* **460**, 1101–1105 (2009).

41. Jung, W. et al. Warping effects in the band and angular-momentum structures of the topological insulator Bi_2Te_3. *Phys. Rev. B* **84**, 245435 (2011).

42. Fu, L. Hexagonal warping effects in the surface states of the topological insulator Bi_2Te_3. *Phys. Rev. Lett.* **103**, 266801 (2009).

43. Liu, C.-X. et al. Model Hamiltonian for topological insulators. *Phys. Rev. B* **82**, 045122 (2010).

44. Chen, Y. L. et al. Experimental realization of a three-dimensional topological insulator, Bi_2Te_3. *Science* **325**, 178–181 (2009).

45. Zhang, H. et al. Topological insulators in Bi_2Se_3, Bi_2Te_3 and Sb_2Te_3 with a single Dirac cone on the surface. *Nat. Phys.* **5**, 438–442 (2009).

46. Alpichshev, Z. et al. STM imaging of electronic waves on the surface of Bi_2Te_3: topologically protected surface states and hexagonal warping effects. *Phys. Rev. Lett.* **104**, 016401 (2010).

47. Kasai, S. et al. Modulation of effective damping constant using spin Hall effect. *Appl. Phys. Lett.* **104**, 092408 (2014).

48. Hirayama, S., Mitani, S., Otani, Y. & Kasai, S. Direct current modulation of spin-Hall-induced spin-torque ferromagnetic resonance in platinum/permalloy bilayer thin films. *J. J. Appl. Phys.* **57**, 060301 (2018).

49. Fu, Q. et al. Observation of nontrivial spin-orbit torque in single-layer ferromagnetic metals. *Phys. Rev. B* **105**, 224417 (2022).

50. Liu, L. Q. et al. Spin-torque switching with the giant spin Hall effect of tantalum. *Science* **336**, 555–558 (2012).

51. Pai, C.-F. et al. Spin transfer torque devices utilizing the giant spin Hall effect of tungsten. *Appl. Phys. Lett.* **101**, 122404 (2012).

52. Liu, Y.-T. et al. Field-free type-x spin-orbit-torque switching by easy-axis engineering. *Phys. Rev. Appl.* **18**, 034019 (2022).

53. Xue, F. et al. Field-free spin-orbit torque switching assisted by in-plane unconventional spin torque in ultrathin [Pt/Co]$_N$. *Nat. Commun.* **14**, 3932 (2023).

54. Winkler, M. et al. Electrical and structural properties of Bi_2Te_3 and Sb_2Te_3 thin films grown by the nanoalloying method with different deposition patterns and compositions. *J. Mater. Chem.* **22**, 11323–11334 (2012).

55. Liu, W., Stoica, V., Chi, H., Endicott, L. & Uher, C. Epitaxial growth and improved electronic properties of $(Bi_{1-x}Sb_x)_2Te_3$ thin films grown on sapphire (0001) substrates: the influence of Sb content and the annealing. *J. Alloys Compd.* **647**, 50–56 (2015).

56. Naumochkin, M., Park, G.-H., Nielsch, K. & Reith, H. Study of the annealing effects of sputtered Bi_2Te_3 thin films with full thermoelectric figure of merit characterization. *Phys. Status Solidi* **16**, 2100533 (2022).

57. Robbie, K. & Brett, M. J. Sculptured thin films and glancing angle deposition: growth mechanics applications. *J. Vac. Sci. Technol. A* **15**, 1460–1465 (1997).

Acknowledgements

Author contributions

Y.T. conceived the project. S.S. planned and performed the experiments. Y.A. developed the theoretical models with input from J.I. S.S. analyzed the data with input from S.K. All the authors discussed the results. S.S., Y.A., J.I., and S.K. wrote the manuscript.

Competing interests

The authors declare no competing interests.

Additional information

Supplementary information The online version contains supplementary material available at https://doi.org/10.1038/s42005-025-02024-1.

Correspondence and requests for materials should be addressed to Shinya Kasai.

Peer review information *Communications Physics* thanks Emanuele Longo and the other, anonymous, reviewer(s) for their contribution to the peer review of this work.

Reprints and permissions information is available at http://www.nature.com/reprints

Publisher's note Springer Nature remains neutral with regard to jurisdictional claims in published maps and institutional affiliations.